Identification of Defect Prone Peritectic Steel Grades by Analyzing High-Temperature Phase Transformations

PETER PRESOLY, ROBERT PIERER, and CHRISTIAN BERNHARD

Continuous casting of peritectic steels is often difficult and critical; bad surface quality, cracks, and even breakouts may occur. The initial solidification of peritectic steels within the mold leads to formation of surface depressions and uneven shell growth. As commercial steels are always multicomponent alloys, the influence also of the alloying elements besides carbon on the peritectic phase transition needs to be taken into account. Information on the solidification sequence and phase diagrams for initial solidification are lacking especially for new steel grades, like high-alloyed TRIP-steels with high Mn, Si, and particularly high Al contents. Based on a comprehensive method development, the current study shows that differential scanning calorimeter measurements allow a clear prediction if an alloy is peritectic (*i.e.,* critical to cast). In order to confirm these results, thermo-optical analyses with a high-temperature laser-scanning-confocal-microscope are performed to observe the phase transformations in situ up to the melting point.

I. INTRODUCTION

IT is well known that the production of specific steel grades by means of continuous casting (CC) is often difficult and critical; bad surface quality cracks and even breakouts may occur. Particularly, the formation of surface depressions during the initial solidification within the mold can be obtained at a certain range of carbon. This is illustrated in Figure 1(a) in terms of an unevenness index which is defined as $\Delta d/l$ (Δd is the differences between neighboring maximums and minimums on the strand surface; l is the interval of these two points).[1,2] The more uneven the shell, the larger is $\Delta d/l$. A maximum is reached at approximately 0.12 C wt pct. Depression formation further results in uneven shell growth, coarse grains, and other negative events such as the formation of hot tears.

Figure 1(b) shows hot tears at different positions below a depression and represents a critical material defect which results in a significant loss of quality. The formation of hot tears in the base of depressions is related to the air gap formation, the resulting lower heat transfer from the mold, a thinner strand shell, and the increases in stresses and strains in the solid/liquid (S/L) two-phase region. These correlations are explained in detail in the literature.[3,4] The depression formation during the CC process is described by means of examples in[5–8] and is mainly determined by the chemical composition of the melt. Steels with an equivalent carbon content between 0.09 and 0.17 clearly show a maximum number of these negative phenomena. Besides depression formation, comparatively higher mold level fluctuations and surface temperature variations are typical phenomena in casting of steels within this critical carbon range.

Phase diagrams and the knowledge of phase transformations of materials represent important information for scientists, materials engineers, and process operators to understand the material behavior during solidification and the whole further processing. Considering the high-temperature range of the iron-carbon (Fe-C) equilibrium phase diagram, illustrated in Figure 2(a), the above mentioned critical/specific steel grades range between the characteristic points C_A and C_B. Upon classifying four different carbon ranges (range I left of C_A, range II between C_A and C_B, range III between C_B and C_C, and range IV right of C_C), a clearly different solidification and transformation sequence is experienced. Table I summarizes the differences in the transformation behavior in the equilibrium binary Fe-C system. Special features are the two different high-temperature phases: δ- and γ-iron, showing significant differences in their densities because of the diverse crystal structure (δ = face-centered cubic/γ = body-centered cubic).[9]

The position of the characteristic point C_A in the pure Fe-C system is given from 0.088[10] to 0.1[11] C wt pct. Here, reliable sources and ThermoCalc 5.0 (Database: FCFE 6) mainly specify 0.09.[12,13] For the point C_B, a value of 0.17[12,13] is given, while the published range is specified from 0.16[11] to 0.18[14] C wt pct.

Steels solidifying according to the range II transformation sequence are of special interest compared with the

PETER PRESOLY, Research Associate, Chair of Ferrous Metallurgy, and CHRISTIAN BERNHARD, Associate Professor, Chair of Ferrous Metallurgy, are with the Montanuniversitat Leoben, Franz-Josef-Straße 18, A-8700 Leoben, Austria. Contact e-mail: peter.presoly @unileoben.ac.at ROBERT PIERER, Research Associate, formerly with the Montanuniversitat Leoben, is now with the INTECO Special Melting Technologies GmbH, A-8600 Bruck an der Mur, Austria.

other three ranges, because in this case, the transformation of δ-Fe to γ-Fe (i.e., the peritectic phase transition $L + \delta \rightarrow \gamma$) coincides with the final solidification and ends in the solid. It is believed that this specific transformation sequence during solidification and subsequent cooling is responsible, as previously described, for more defect appearances in the CC process (such as hot tears, surface defects, depression formation, and in the worst case breakouts).

Since steel is made of a multicomponent material alloying elements, which significantly influence the phase diagrams and the position and temperature of the characteristic points C_A, C_B, and C_C have to be considered. This situation is demonstrated in Figure 2(b) in terms of a pseudo-binary Fe-C diagram. The effect of the alloying elements can be distinguished between austenite formers (like Mn, Ni, Cu, etc.) and ferrite formers (like Cr,

Mo, Al, etc.). It can also be seen that the presence of higher concentrations of alloying elements prefer the formation of a peritectic ternary region ($L + \delta + \gamma$). Great efforts were made in the past to describe the influence of alloying elements on the transformation sequence with calculation methods. For process operators of CC machines, it is very important to identify if a specific steel grade is within the critical range II. If the sequence of phase transformations and the characteristic points C_A and C_B are well known, then critical steel grades can be produced safely by target selection of special casting powders, cooling programs and casting speed.[15,16]

Therefore, reliable investigations are essential to find out whether a new steel grade is within the critical range (i.e., between C_A and C_B). In addition, the transformation behavior needs to be characterized in detail. This question goes hand in hand with the search for a reliable
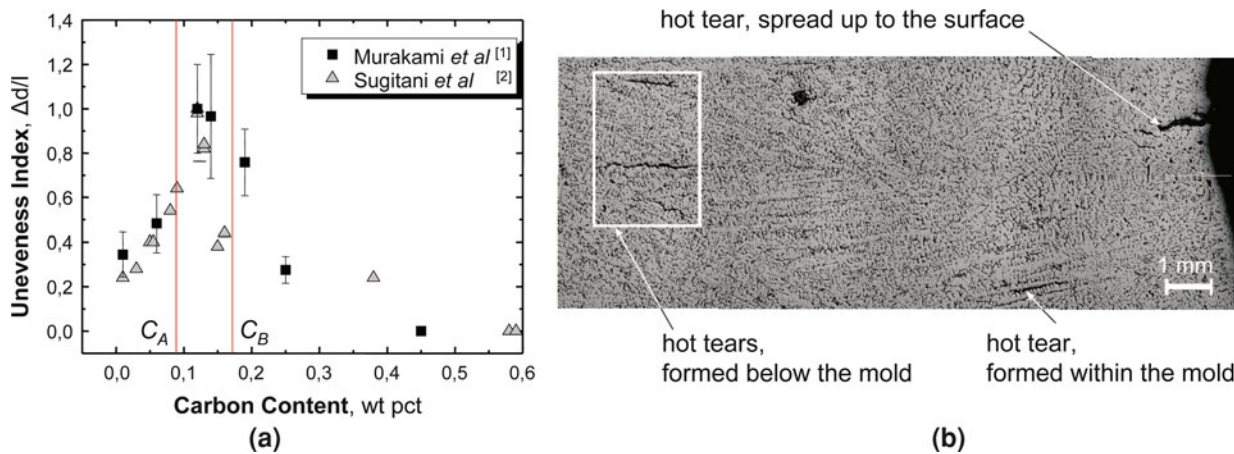

Fig. 1—(a) Unevenness index over the carbon content,[1,2] and (b) different types of hot tears as a result of a depression.[3]
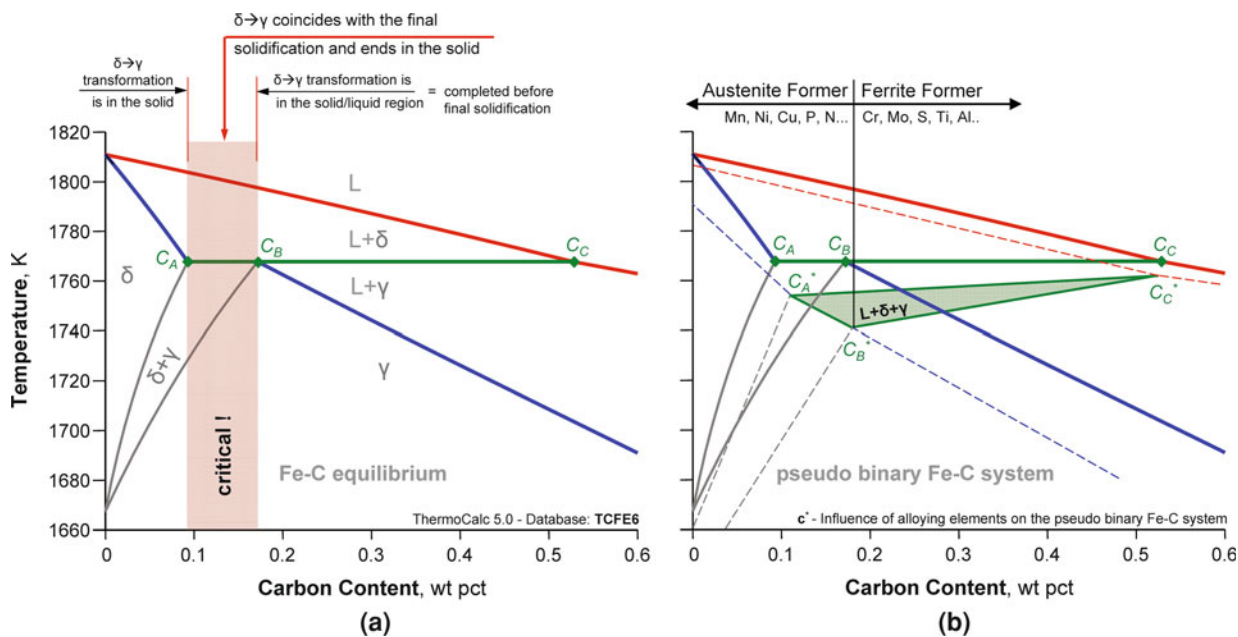

Fig. 2—(a) Fe-C equilibrium diagram with the critical carbon range between 0.09 and 0.17 wt pctC, and (b) influence of alloying elements on the Fe-C system.

Table I. Different Transformation Characteristics in the Fe-C System

Range	Position	Phase Sequence	Characteristics
I	left of C_A	$L \rightarrow L + \delta \rightarrow \delta \rightarrow \delta + \gamma \rightarrow \gamma$	primary δ-Fe solidification
II	between C_A and $C_B =$ hypo-peritectic	$L \rightarrow L + \delta \rightarrow \delta + \gamma \rightarrow \gamma$	peritectic transformation coincides with the final solidification
III	between C_B and $C_C =$ hyper-peritectic	$L \rightarrow L + \delta \rightarrow L + \gamma \rightarrow \gamma$	peritectic transformation occurs in the solid/liquid two-phase region
IV	right of C_C	$L \rightarrow L + \gamma \rightarrow \gamma$	primary γ-Fe solidification

and simple laboratory method. In the current study, DSC measurements are used. In order to confirm these results, thermo-optical analyses with a high-temperature HT-LSCM are performed to observe the phase transformations in situ up to the melting point.

In the following sections, different calculation methods to characterize peritectic steel grades (between C_A and C_B) are summarized. The potential of DSC and HT-LSCM measurements to characterize the different transformation characteristics are illustrated based on three different alloys from the ternary system Fe-C-1Si wt pct. Finally, the above described approaches are applied, using the example of a new Fe-0.22C-2Al wt pct alloy. It is demonstrated that one DSC measurement is sufficient to determine the transformation characteristics and to define whether an unknown steel grade is in range I, II (critical), III, or IV. This is carried out by illustrating and discussing the measured DSC signal in comparison with thermo-optical analyses of the microstructure in the same temperature range.

II. CALCULATION METHODS AND MODEL ALLOYS

In the following sub-sections, four different methods to calculate the influence of alloying elements on the transformation characteristics are summarized. All these methods are tools to characterize steel grades regarding the peritectic phase transformation on the basis of the alloy composition. The first three methods are typical practical tools for industrial CC production.

A. Carbon Equivalent Calculations

The most widely used method is to calculate the equivalent carbon content (C_P) by adding up the composition of different alloying elements (C_i) in wt pct with dimensionless weighting coefficients (X_i), where austenite formers are always positively weighted (shift to the right in the Fe-C-system) and ferrite formers negatively. If the calculated value of C_P is between 0.09 and 0.17 ($= C_A$ and C_B in the binary Fe-C system), then the steel is considered as "peritectic and prone to cracks and depressions." C_P-formulas were published by several authors[17–19] and can—in a generalized form—be written as Eq. [1]:

$$C_P = C_C + \sum_{i=1}^{i=n} X_i^* C_i \quad \text{for example:}$$

$$C_P = [\text{pct C}] + X_{Mn} * [\text{pct Mn}] - X_{Si} * [\text{pct Si}] + \cdots \quad [1]$$

Such additive C_P-formulas often originate not only from the consideration of binary systems but also from operational observations and describe low-alloyed carbon steels well. However, such simple approaches cannot consider the interaction between the different elements which is relevant for higher-alloyed steels grades; here, the use of these formulas might result in unrealistic values.

B. Calculation Model from Kagawa and Okamoto

The approach by Kagawa and Okamoto[20] considers the influence of alloying elements on the critical points C_A, C_B, and C_C in a more fundamental way. The model is based on coefficients reflecting the shift in the temperatures (ΔT_{CA}, ΔT_{CB}, and ΔT_{CC}) and concentrations (ΔC_{CA}, ΔC_{CB}, and ΔC_{CC}) of the critical points for each element. With this information, even full pseudo-binary Fe-C equilibriums in consideration of all possible high-temperature phase transformations can be calculated, as well as the concentrations and temperatures of C_A^*, C_B^* and C_C^*, like in Figure 2(b). This more comprehensive model considers the different effects of third elements on the critical points, particularly the distance between C_A and C_B ($=$ range II) can expand. As for methods described in Sections II–A and II–C, the coefficients are only valid for a limited concentration range.

C. Peritectic Predictor Equations from Blazek et al.[21]

The peritectic predictor equations are two formulas, respectively, for C_A (Eq. [2]) and C_B (Eq. [3]) and were published by Blazek et al.[21]:

$$\begin{aligned}
C_A = {}& 0.0896 + 0.0458 * \text{Al} - 0.0205 * \text{Mn} \\
& - 0.0077 * \text{Si} + 0.0223 * \text{Al}^2 - 0.0239 * \text{Ni} \\
& + 0.0106 * \text{Mo} + 0.0134 * \text{V} - 0.0032 * \text{Cr} \\
& + 0.00059 * \text{Cr}^2 + 0.0197 * \text{W} \quad [2]
\end{aligned}$$

$$\begin{aligned}
C_B = {}& 0.1967 + 0.0036 * \text{Al} - 0.0316 * \text{Mn} \\
& - 0.0103 * \text{Si} + 0.1411 * \text{Al}^2 - 0.05 * \text{Al} * \text{Si} \\
& - 0.0401 * \text{Ni} + 0.03255 * \text{Mo} + 0.0603 * \text{V} \\
& - 0.0024 * \text{Cr} + 0.00142 * \text{Cr}^2 + 0.0197 * \text{Cr} * \text{Ni} \\
& + 0.0266 * \text{W}
\end{aligned}$$

These formulas are based on a comprehensive regression study of the influence of alloying elements on the

critical points C_A and C_B, using the commercial thermodynamic software ThermoCalc (Version M) within a certain concentration range (*e.g.*, Mn, Si, and Al up to maximum 2 wt pct). The formulas are similar to C_P-formulas: Austenite formers are rated negatively and ferrite formers (with the exception of silicon) are rated positively. A great advantage in comparison with previous C_P-formulas is that C_A and C_B are given separately and also the partial interaction of selected elements, such as Al*Si and Ni*Cr, is considered.

D. *CALPHAD Method—Gibbs Minimizer*

The most comprehensive method is the numerical calculation of multicomponent phase diagrams using the CALPHAD approach which considers all (known) interactions. There are different commercial Gibbs minimizers available in the market, such as ThermoCalc[12] (TC), FactSage[10] (FS), MTDat,[22] PANDAT,[23] and so on. All these programs are only as good as the underlying databases, which are based exclusively on previously measured alloy systems. Figure 3 shows, for example, the results of calculated pseudo-binary Fe-C-1Si (left) and Fe-C-1Al wt pct (right) diagrams using ThermoCalc 5.0 and FactSage 6.2. The results of the TC and FS calculations show very good agreement (*i.e.*, all differences in the transformation temperatures ΔT are smaller than 10 K) in the case of Fe-C-1Si alloy, but contradictory results in the case of Fe-C-1Al wt pct. One explanation is that for the ternary description of the Fe-C-Si system, both databases (TCFE6 and FSstel) use the same primary source from Lacaze *et al.*[24] and Miettinen.[25] However, for the ternary Fe-C-Al system only the ThermoCalc database (FCFE6) uses a thermodynamic description from Connetable *et al.*,[26] based mainly on ab initio calculations.

For typical low-alloyed Fe-C-Si-Mn steels (common construction and engineering steel grades with *e.g.*, up to 0.3Si and 1.5Mn wt pct), all four different methods (Section II–A to II-D) usually agree very well. Even

simple C_P calculations (Section II–A) excellently describe these typical low-alloyed steel grades. For higher-alloyed steels, Sections II–C and II–D are recommended. Higher-alloyed complex steel grades (*e.g.*, TRIP-steels) are particularly difficult to predict and need further study.

III. EXPERIMENTAL MATERIALS AND METHODS

In the following section, the two applied experimental methods, DSC and HT-LSCM, are described. Before that, the selected model alloys for the experimental studies are summarized.

A. *Model Alloys for the Experimental Studies*

In order to demonstrate the potential of the DSC and HT-LSCM methods, three model alloys (Alloy-1 to -3) from the well-known Fe-C-1Si wt pct system are investigated and discussed (shown in Figure 3 left and summarized in Table II). Then an alloy (Alloy-4), included in the phase diagrams in Figure 4, from the ternary system Fe-C-Al is analyzed with both methods. Alloy-4 with a composition of Fe-0.22C-2Al wt pct was chosen purposely, because the commercial thermodynamic databases, TCFE6 and FSstel, show contradicting results for this alloying system. Furthermore, a carbon content of 0.22 wt pct and an aluminum content of 2 wt pct are typical for some commercial TRIP-steels.

Table II. Model Alloys, Chemical Composition in Weight Percent

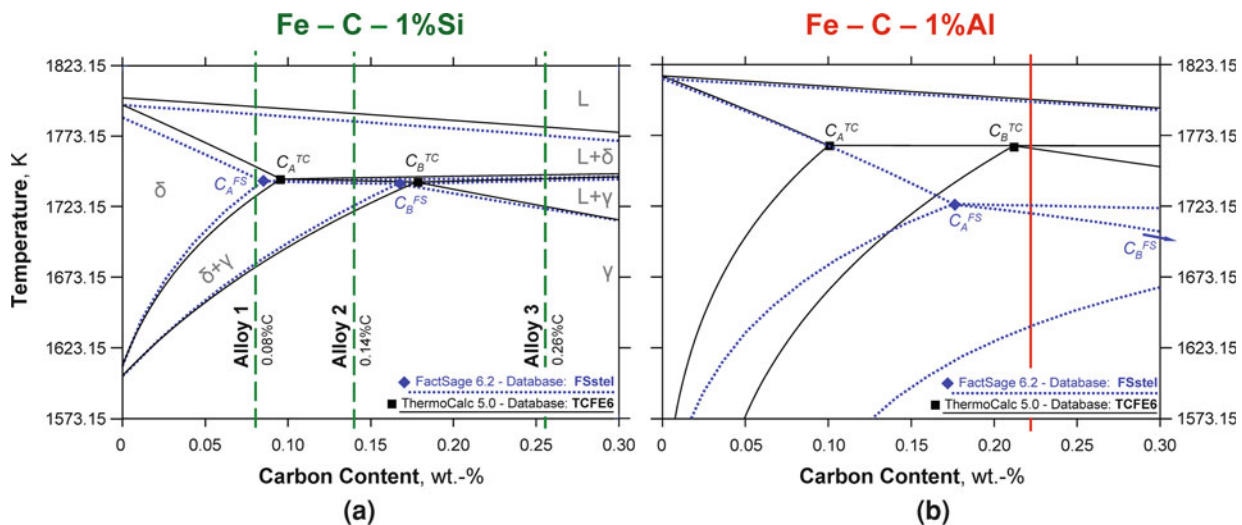| Alloy	Carbon	Silicon	Aluminum	Iron
1	0.084	0.99	—	balance
2	0.142	0.98	—	
3	0.256	0.99	—	
4	0.224	—	1.97	

Fig. 3—ThermoCalc and FactSage calculation of the pseudo-binary Fe-C diagram of the system Fe-C-1 pct Si (*left*) and Fe-C-1 pct Al (*right*).
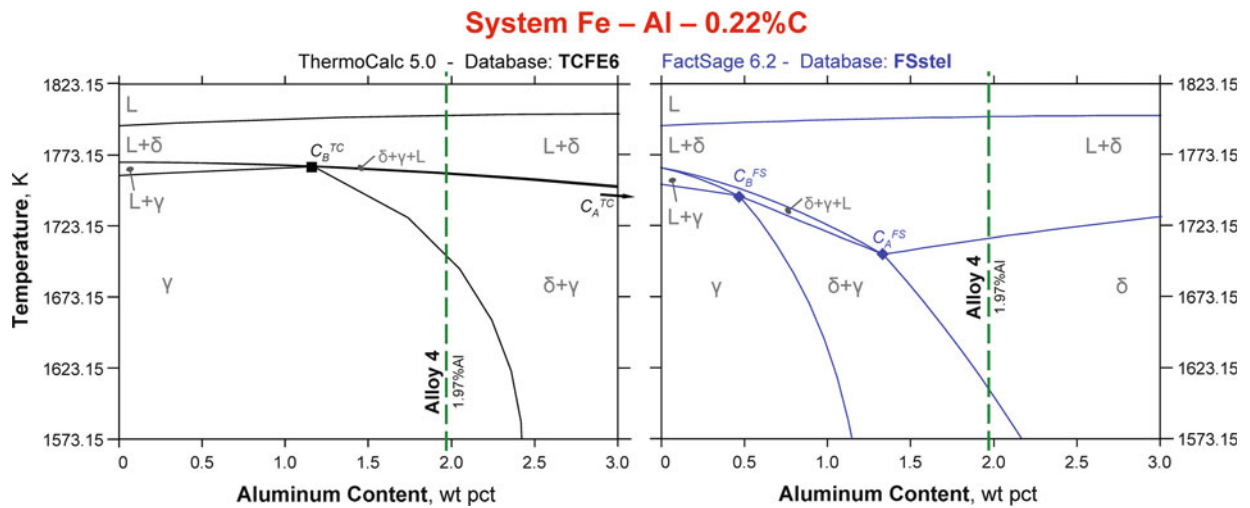
Fig. 4—Thermodynamic calculations of the pseudo-binary Fe-Al system.

The model alloys (about 60 g) were melted from high-purity raw materials in an alumina crucible with a High-Frequency Remelting Furnace (HRF) under argon atmosphere 5.0 and were centrifugally cast in a copper mold. The samples are very homogeneous because of inductive melting, centrifugal casting, and the extremely rapid solidification in the copper mold. The alloy composition was analyzed by emission-spectroscopy and is summarized in Table II. The only significant trace element was Mn with a content of 0.023, while the total level of all other trace elements was below 0.03 wt pct. All trials (DSC and HT-LSCM) were performed using material from the same sample.

B. Differential Scanning Calorimeter (DSC)

DSC measurements are an excellent method to record all transitions associated with an exo- or endothermic effect (= enthalpy change). Detailed descriptions of the DSC technique can be found for example in.[27,28] The equipment used in the study was a NETZSCH STA409PG *Luxx* (Simultaneous Thermal Analyzer, Selb, Germany) with a platinum DSC sensor and type-S thermocouples as shown in Figure 5. The experimental set-up was calibrated by measuring the well-known melting points of high-purity In, Sn, Al, Ag, Au, Ni, and Co. The standard deviation of the temperature measurements was determined for solid–solid transitions (low enthalpy change) with ±3 K and for solid–liquid transitions (high enthalpy change) with ±1.5 K. All measurements were carried out under the same conditions in alumina crucibles with lids under protective gas atmosphere (argon, quality 6.0) with a flow of 30 cm^3 $minutes^{-1}$ during controlled heating up to 1823.15 K (1550 °C). In order to achieve the best equilibrium conditions, ground 50 mg samples and a heating rate of 10 K/minutes were used.

In addition, thermal resistance and the time constants of the measurement system were corrected by an extra calculation with the Netzsch Programm Correct2.[29] Accurate measurements of highly reactive steels with higher amounts of Al and Si require special attention

regarding the purity of the atmosphere in the DSC and their leak tightness. During all trials, the thermogravimetric (TG) function of the STA409 was used to control the sample mass, but since the DSC sensor could move freely in the furnace chamber through the balance function, no qualitative heat flow measurements could be made. Therefore, the DSC-signal is only specified in μV/mg. The use of the TG-function for these highly reactive alloys is very important, because any increase of the sample mass is an indication of oxidation, thus resulting in an invalid measurement result. For this reason, the full system is evacuated and purged with argon three times before each measurement. Furthermore, Ti and Zr getters are used to clean the protective gas in the oven.

C. High-Temperature Laser-Scanning-Confocal-Microscopy (HT-LSCM)

The high-temperature laser-scanning-confocal-microscopy is a special kind of thermo-optical analysis (TOA) which enables in situ observations of surface phenomena in liquid and solid samples up to a maximum temperature of 1923.15 K (1650 °C). The HT-LSCM applied in the study was a YONEKURA VL 2000 DX with SVF17SP using a blue laser beam, because its wavelength is out of the spectra of the sample radiation at high temperatures. This allows for high-quality images of the microstructure with a resolution below 1 μm (corresponding to a 400 times—magnification). Since this well-established method is described in detail in the relevant literature,[30–33] the current study only gives a brief overview on the experimental set-up. Figure 6 shows the principle design of the used HT-LSCM together with detailed images of the sample holder in the high-temperature furnace. This infrared furnace consists of a gold-coated chamber and has the shape of a symmetric ellipse. The heating is carried out by means of a halogen lamp located in the bottom focal point, whereas the crucible is in the upper focal point.

Similar to other thermal analysis methods, protective gas atmosphere (argon, quality 6.0), type-S thermocou-
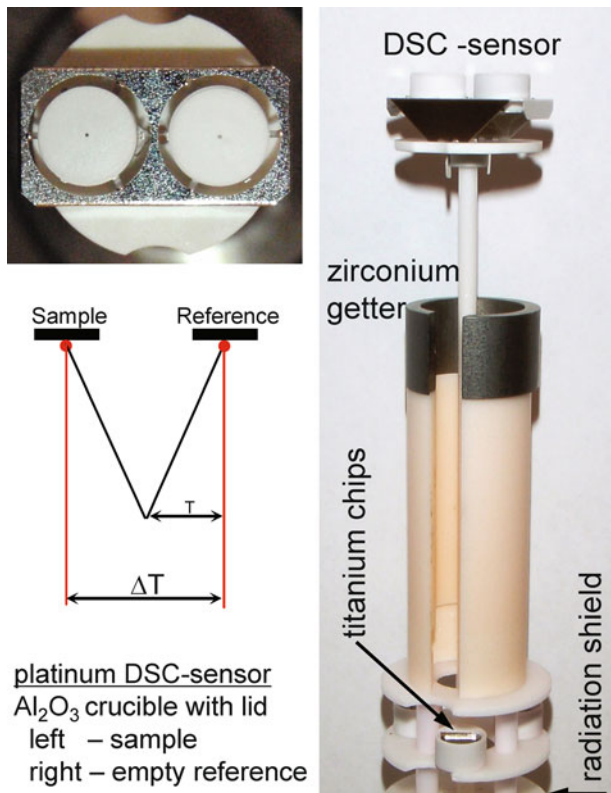
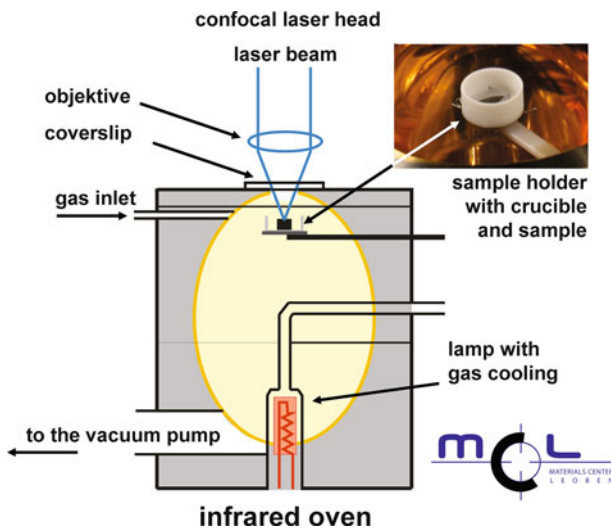Fig. 5—Layout of a high-temperature DSC sensor with Zr and Ti getters.

Fig. 6—Principle design of the used HT-LSCM.

ples in the Pt-sample holders and alumina crucibles were used. In the current study, the following experimental adjustments and parameters were employed. The sample size was 4 × 4 × 1 mm (polished, but not etched). The heating rate was 500 K/minutes up to a temperature of 1573.15 K (1300 °C). Subsequently, an isothermal holding took place for 5 minutes being followed by a slow heating up using a heating rate of 10 K/minutes until everything on the surface was liquid. During the experiment, a video was produced (60 frames per second) to

observe even fast processes. This video was analyzed in detail, and the results are illustrated in the next section. Phelan et al.[33] showed that observations made on the sample surface are also representative for the bulk behavior. A further great potential of HT-LSCM trials are kinetic studies like investigations of grain growth, solidification, sub-cooling, and time–temperature-transformations. The disadvantage of the HT-LSCM is the increased deviation in the temperature determination, which in addition depends on the temperature level and even on the sample properties, like the absorption factor of the material. Furthermore, the temperature cannot be calibrated as easily as in the DSC, therefore the expected standard deviation is in the range of ±5 K.

IV. RESULTS AND DISCUSSION

In Section IV–A, the potential and the limitations of the two different experiment methods DSC and HT-LSCM will be discussed on the basis of the experimental results for three different model alloys (Alloy-1, -2 and -3 in Figure 3) from the Fe-C-1Si wt pct system. The fundamental types of the phase transformation sequence during melting (Table I) result in different DSC signal characteristics, as explained in detail later on. In Section IV–B, Alloy-4 Fe-0.22C-2Al wt pct is analyzed with the four methods described in Section II and then the calculation results are compared with the results of DSC studies.

All experiments (DSC and HT-LSCM) were performed under comparable conditions as near-equilibrium, low heating rate (10 K/minutes) experiments in the high-temperature range. Each sample was heated up only one time to prevent any influence of oxidation on the sample composition and thus on the DSC signal. Cooling experiments for the investigated alloys show very strong super cooling influence and poor reproducibility. Since phase transformations are always associated with a change in enthalpy (i.e., heat will be released or consumed), a phase transformation results in a deviation of the horizontal baseline. The illustrated DSC curves (DSC-signal^{corr}), i.e., the measured heat flow, are adjusted by the influence of the heating rate, sample mass, crucible, and DSC-sensor configuration. This signal correction procedure (using a commercial software tool[29]) identifies the determined temperatures as equilibrium transformation temperatures (corresponding to a heating rate of 0 K/minutes). In addition, the transformation temperatures and the stability range of phases are illustrated together. Identification of the appearing phases is a complex task and has to be supported by the interpretation of HT-LSCM observations. Significant transformation temperatures from the DSC measurement are depicted as red dots. The apparent temperatures for the corresponding HT-LSCM observations are marked with black arrows.

A. Experimental Results of the Fe-C-1Si Alloys-1 to -3

1. Alloy-1 Fe-0.08C-1Si (left of C_A = range I)

In Figure 7, the detailed findings for Alloy-1 are compiled and depicted versus temperature. During the
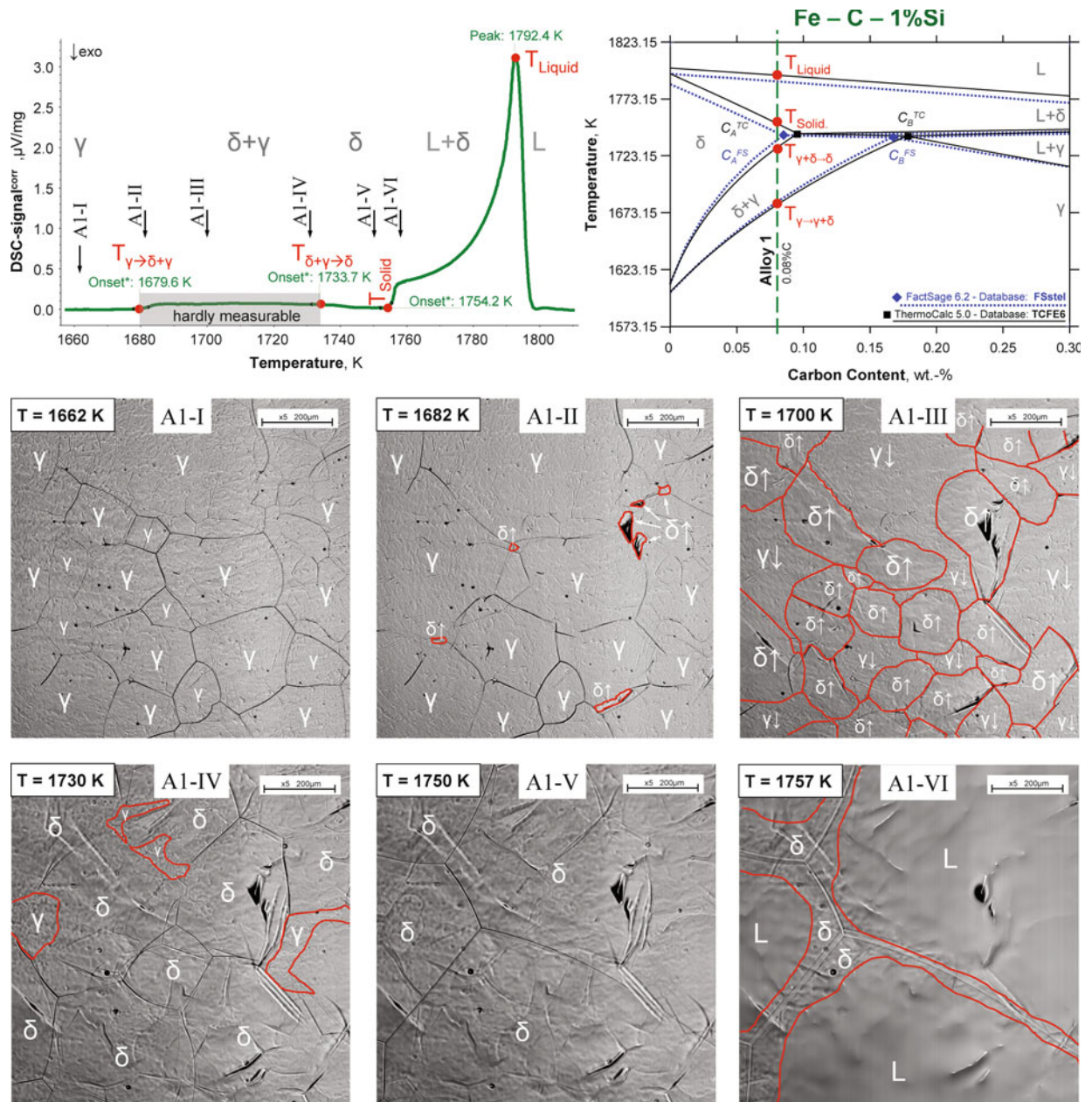
Fig. 7—DSC and HT-LSCM measurements of Alloy-1 (Fe-0.08C-1Si wt pct).

heating up from 1573.15 K to 1679.65 K (1300 °C to 1406.5 °C) no transformation is observed. The DSC signal shows a flat baseline and the HT-LSCM photomicrographs a 100 pct γ-grain microstructure with significant grain growth, noticeable in subimage A1-I and A1-II in terms of consumption of all smaller γ-grains. The first deviation from the DSC baseline is observed at 1679.65 K (1406.5 °C). However, only a very smooth increase of the heat flow can be observed which indicates a transformation with only very small enthalpy changes. This is typical for the austenite to δ-ferrite transformation $(\gamma \rightarrow \gamma + \delta)$ which starts at 1679.65 K (1406.5 °C). The larger the temperature range of the two-phase region $(\gamma + \delta)$, the smaller the heat flow per unit of time. Consequently, the $\gamma \rightarrow \delta$ transformation is hardly measurable by DSC.

HT-LSCM is particularly useful to observe the formation of δ-ferrite, which starts at the γ grain boundaries and triple points, shown in subimage A1-II. Upon further heating, the phase fraction of the δ phase increases, while the γ phase fraction decreases (subimage A1-III and A1-IV). The newly formed δ phase can be identified by its smooth surface compared with the structured surface of the preexisting γ grains. At 1733.75 K (1460.6 °C), the DSC signal decreases slowly and a straight baseline is resumed again. This indicates that the $\gamma \rightarrow \delta$ transformation is completed, and only δ-ferrite is left. The presence of 100 pct δ-ferrite is confirmed by the HT-LSCM subimage A1-IV, which shows the large, newly formed δ grains. The temperature of the melting onset $(= T_{Solid})$ corresponds to 1754.25 K (1481.1 °C). The characteristics of the DSC signal between solidus and liquidus are typical for binary or multicompo-

nent alloys with an explicit two-phase (S/L) area. The DSC signal peak at 1972.45 K (1519.3 °C) corresponds to the liquidus temperature ($= T_{Liquid}$). The appearance of first melted phases can be identified very clearly with the HT-LSCM. Upon further heating, the melt spreads over the whole surface as shown in subimage A1-VI. After complete melting of the sample, the non-wetting system, steel/alumina, results in the formation of a steel droplet, preventing further HT-LSCM observations. It is therefore not possible to determine the liquidus temperature adequately with the use of the HT-LSCM method.

The DSC and HT-LSCM studies clearly determined a transformation sequence of $\gamma \rightarrow \gamma + \delta \rightarrow \delta \rightarrow L + \delta \rightarrow L$ ($=$ range I) for Alloy-1. Both methods complement each other. The DSC measurements show that the basic assessment of Alloy-1 as primary ferritic solidifying steel by both TC and FS calculations is correct. The deviations between the two calculations and the measurement are below ± 5 K, except the FS calculation of T_{solid} which is more than 10 K too low. The DSC signal from alloys left of C_A (range I—primary δ-Fe solidification) and alloys right of C_C (range IV—primary γ-Fe solidification) show similar melting characteristics, except the width of the two-phase S/L-region, which is much wider at higher carbon contents. Also alloys from range I show a complete $\gamma \rightarrow \delta$ transformation before melting.

2. Alloy-2 Fe-0.14C-1Si (between C_A and C_B = range II)

Figure 8 shows the results for Alloy-2. At first, the characteristics of the DSC signal are very similar to that for Alloy-1 (subimages A2-I, -II, and -III, similar to
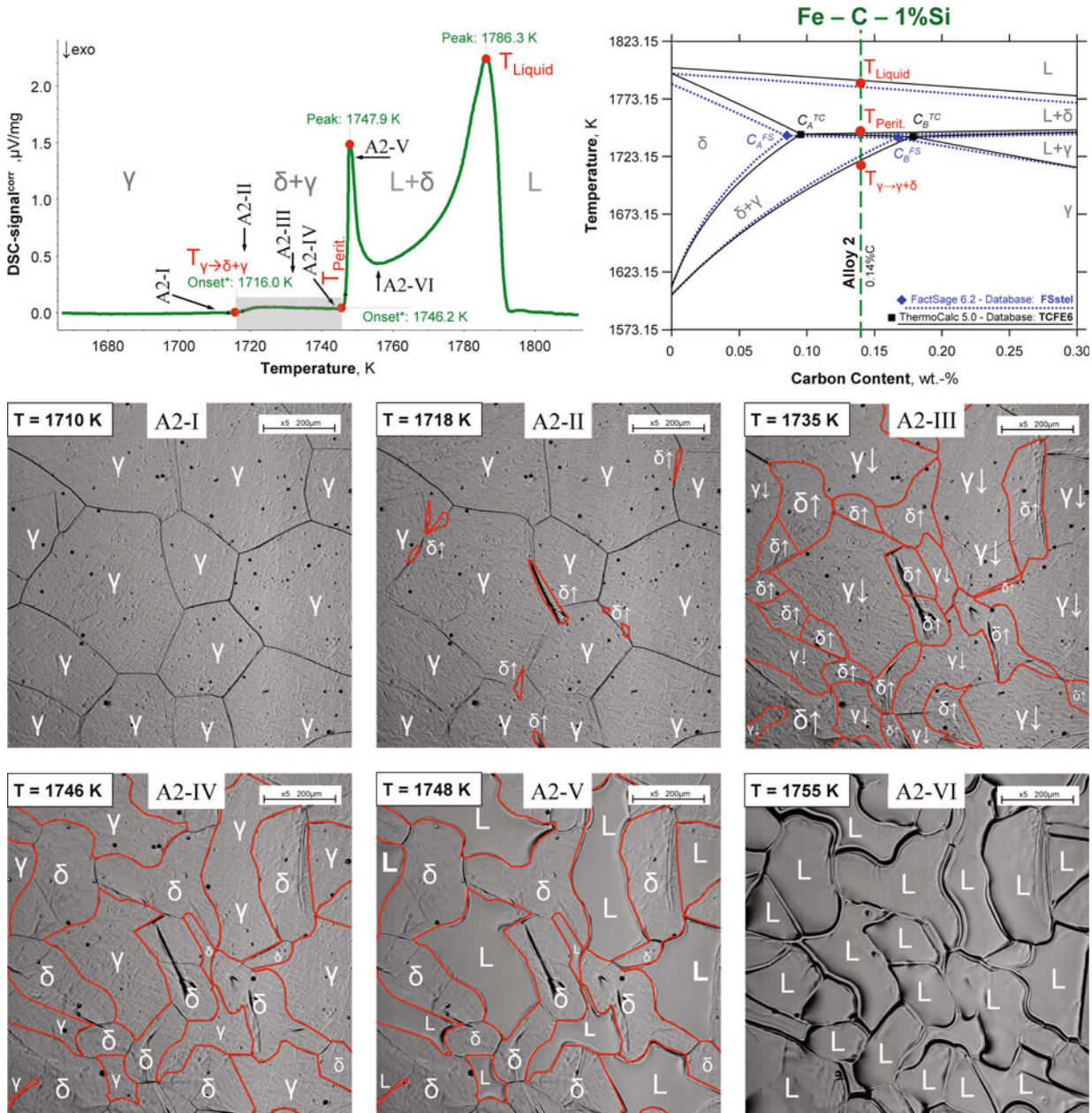

Fig. 8—DSC and HT-LSCM measurements of Alloy-2 (Fe-0.14C-1Si wt pct).

subimages A1-I, -II, and -III). The first deviation from the DSC baseline, indicating the start of the δ-ferrite formation ($\gamma \rightarrow \gamma + \delta$), occurs at 1716.05 K (1442.9 °C). Upon further heating, the phase fraction of the δ phase increases, while the γ phase fraction decreases (subimages A2-III and -IV). At 1746.25 K (1473.1 °C), a very sharp peak appears in the DSC signal, reaching a maximum value at 1747.95 K (1474.8 °C). The onset of this peak can be associated with the peritectic phase transformation temperature T_{Perit} and the peak maximum with the end of the transformation $\delta + \gamma \rightarrow L + \delta$. This sharp peak is caused by the enthalpy step of the peritectic phase transformation which coincides in this case with the solidus temperature.

In subimage A2-IV, the HT-LSCM observations show the $\gamma + \delta$ microstructure immediately before the onset of the peritectic phase transformation, which occurs only 2 K higher in subimage A2-V. In subimage A2-V, the former γ phase becomes liquid, while the δ phase remains solid. This observation is the optical evidence of the transformation $\delta + \gamma \rightarrow L + \delta$. Upon further heating, the residual δ phase melts (subimage A2-VI) and the liquid phase spreads over the whole sample surface. The maximum DSC melting peak—corresponding to the liquidus temperature—occurs at 1786.35 K (1513.2 °C). The black dots in the HT-LSCM photomicrographs are small pores in the material and have no influence on the phase transformations.

The DSC and HT-LSCM studies prove a transformation sequence of $\gamma \rightarrow \gamma + \delta \rightarrow L + \delta \rightarrow L$ (= range II)

and confirm that the TC and FS calculations of Alloy-2 are correct. The deviations of the calculated transformation temperatures are below ±5 K, only the FS calculation of $T_{\gamma \rightarrow \gamma + \delta}$ is more than 9 K too high. Referring to Figure 1(a), steels between C_A and C_B (= range II) are most critical. Only these steel grades exhibit a sharp peritectic DSC signal peak, which coincides with the solidus temperature. The HT-LSCM observations show an excellent correspondence with the DSC results.

3. Alloy-3 Fe-0.26C-1 pct Si (between C_B and C_C = range III)

Figure 9 compiles all results for Alloy-3, where no $\gamma \rightarrow \delta$ transformation in the solid occurs, resulting in the flat DSC signal baseline up to the onset of melting. The HT-LSCM observations confirm this by showing a 100 pct γ-grain microstructure with a significant grain growth, but without any new phase formation (subimages A3-I and -II). According to the DSC measurements and the HT-LSCM observations, the onset of melting starts at 1735.05 K (1461.90 °C), visualized in subimage A3-III. As soon as the sample surface is coated with melt, no further HT-LSCM observations are possible. However, the DSC measurement clearly shows that in the two-phase (S/L) area, between T_{Solid} and T_{Liquid}, a separate sharp peak appears at 1746.35 K (1473.2 °C) because of the peritectic phase transformation. When the $L + \gamma \rightarrow L + \delta$ transformation is finished at 1749.65 K (1476.50 °C), the remaining δ-ferrite transforms into liquid, and the DSC signal reaches the
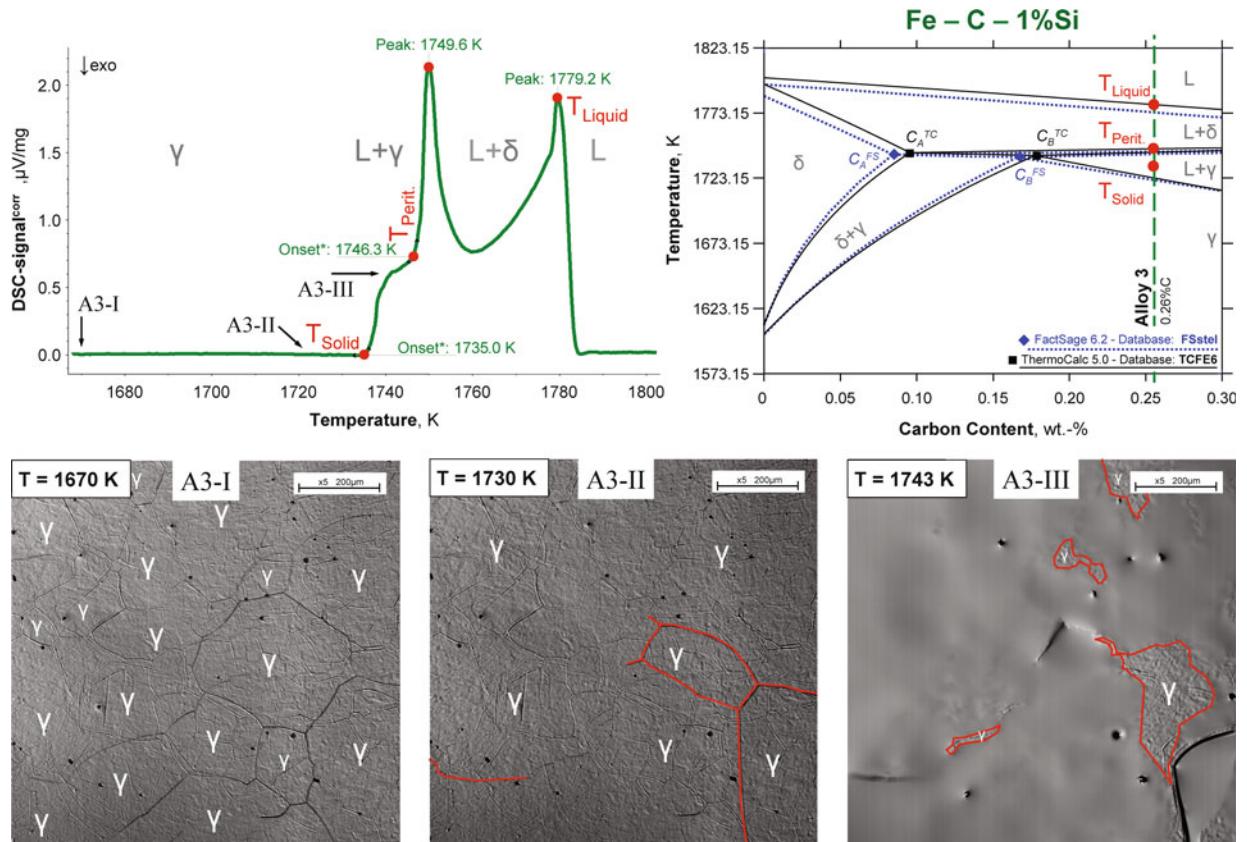

Fig. 9—DSC and HT-LSCM measurements of Alloy-3 (Fe-0.26C-1Si wt pct).

peak maximum at 1779.25 K (1506.1 °C), which corresponds to the liquidus temperature.

The determined transformation sequence for Alloy 3 is $\gamma \rightarrow L + \gamma \rightarrow L + \delta \rightarrow L$ (= range III). The measurements confirm that both the TC and FS calculations for Alloy III are correct, but TC and FS calculations result in T_{Solid} value to be lower by more than 10 K. Alloys which are situated between C_B and C_C also show very clear DSC signal characteristics: The solidus temperature (onset of melting peak) is lower than the separate sharp peritectic peak, which occurs in the two-phase (S/L) area. Another typical feature of alloys between C_B and C_C is the fact that the peritectic peak is higher than the following melting peak.

B. Calculation and Experimental Results of Alloy-4 Fe-0.22C-2Al

The four approaches for the prediction of the phase transformation sequence for steel with a composition close to—or in—the peritectic range, as discussed in Section II, provide contrary results for Alloy-4, as summarized in Table III. As the TC and FS calculations of the Fe-C-Al system show also contradicting results, as shown in Figure 3 (left) and Figure 4, only experimental studies can help us characterize these new alloys.

The DSC measurement and the HT-LSCM subimages, A4-II and -III, compiled in Figure 10, clearly indicate that Alloy-4 is between C_A and C_B (= range II). The

Table III. Results of the Different Prediction Models for Alloy-4

(a) Carbon equivalent calculations
Cannot handle alloys with elevated aluminum content.
If only the carbon content of 0.22 wt pct was considered, the alloy would be in range III.

(b) Calculation model from Kagawa and Okamoto
Cannot handle alloys with elevated aluminum content, the pure Fe-C alloy would be in range III.

(c) Peritectic Predictor Equations from Blazek et al.
The result for the mentioned alloy is $C_A = 0.27$ and $C_B = 0.77$,
Since the alloy has a carbon content of 0.22 wt pct, it is located left of C_A in range I and is not peritectic.
The specified range of validity for aluminum is 0 to 2 wt pct.[21]

(d) Calphad method—Gibbs Minimizer, Fig. 4
For ThermoCalc[12] calculation, range II with a peritectic temperature of 1759.75 K (1486.6 °C).
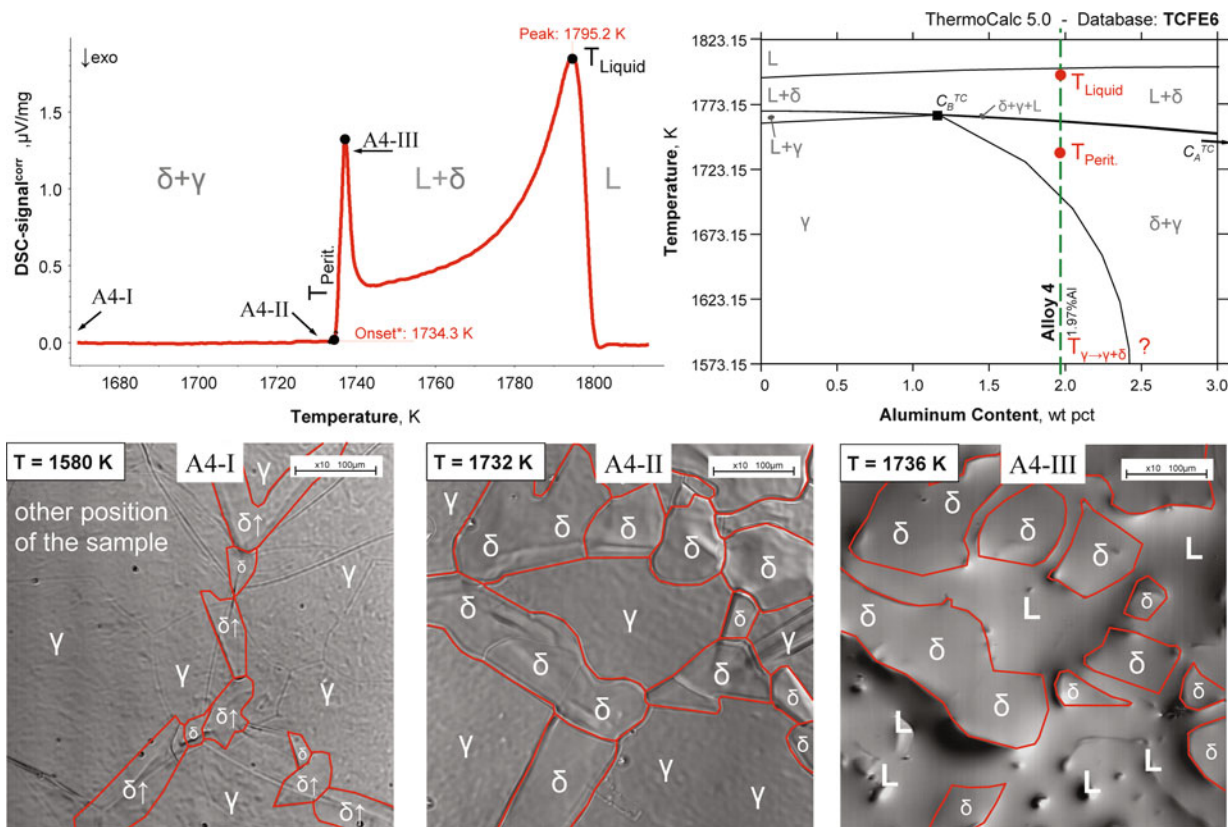For FactSage[10] calculation, range I with a solidus temperature of 1713.65 K (1440.5 °C).

Fig. 10—DSC and HT-LSCM measurements of Alloy-4 (Fe-0.22C-2Al wt pct).

transformation behavior is identified by the sharp peritectic peak, coinciding with the solidus temperature and the observed $\gamma + \delta \rightarrow L + \delta$ transformation (subimage A4-II and -III). This peak only occurs at alloys between C_A and C_B. Therefore, Alloy-4 shows a similar transformation behavior as Alloy-2 (Figure 8). In addition, the DSC measurement shows that the transformation temperature calculated with TC (range II) is more than 25 K too high and that the FS calculations (range I) and the Peritectic Predictor Equations from Blazek *et al.*[21] (range I) show different transformation characteristics.

Further DSC measurements in the Fe-C-Al system are necessary to perform a thorough assessment and to determine the exact position of the critical points C_A and C_B. In the DSC signal (Figure 10), no $\gamma \rightarrow \delta$ transformation can be significantly observed, but the HT-LSCM subimages A4-I and -II clearly show a $\gamma + \delta$ two-phase region. The $\gamma \rightarrow \delta$ phase transformation seems to start at temperature less than 1573.15 K (1300 °C). The enthalpy change of the $\gamma \rightarrow \delta$ transformation is divided up over a temperature of 150 K. The used DSC setup with alumina crucibles does not allow for an identification of this solid–solid transformation.

V. SUMMARY AND CONCLUSIONS

The current study illustrates and discusses high-temperature phase transformations of three different well-known alloys using two laboratory methods, the Differential Scanning Calorimetry (DSC) and the High-Temperature Laser-Scanning-Confocal-Microscope (HT-LSCM). The combination of both methods is a powerful tool and enables the validation and determination of phase diagrams, especially in the high-temperature range.

DSC measurements are an ideal method to measure the solidus, peritectic, and liquidus temperatures with high accuracy. Furthermore, the transformation sequence ($=$ position regarding C_A, C_B, and C_C) can directly be deduced from the measured DSC signal characteristics.

HT-LSCM investigations enable a direct observation (Thermo-Optical Analysis) of the microstructure evolution up to the melting point and provide an optical evidence of the peritectic transformation ($\delta + \gamma \rightarrow L + \delta$).

Owing to small enthalpy changes, DSC results are limited with respect to the $\gamma \rightarrow \delta$ transformation. In addition to the dilatometry and X-ray diffraction methods, the optical in situ observation of phase transformation by HT-LSCM proved to be a comprehensive method.

DSC is an excellent method to determine the peritectic temperature in the S/L region and the liquidus temperature. This cannot be realized using HT-LSCM once the sample surface is fully coated with melt.

Combined DSC and HT-LSCM trials clearly locate Alloy-4 Fe-0.22C-2Al between C_A and C_B ($=$ range II). This contradicts previous results of mathematical prediction models and demonstrates the need for further research activities on steel grades with higher Al contents (like TRIP-steels) and their combinations with additional alloying elements like Si and Mn.

Critical alloys between C_A and C_B ($=$ range II) can be reliably detected with only one DSC trial. This essential information (YES/NO) helps in improving process management of CC and in insuring high product quality.

REFERENCES

1. H. Murakami, M. Suzuki, T. Kitagawa, and S. Miyahara: *Tetsu-to-Hagane*, 1992, vol. 78, pp. 105–11.
2. Y. Sugitani and M. Nakamura: *Tetsu-to-Hagane*, 1979, vol. 65, pp. 1702–11.
3. C. Bernhard: *Berg und Huettenmännische Monatshefte*, 2004, vol. 149, pp. 90–95.
4. R. Pierer, S. Griesser, J. Reiter, and C. Bernhard: *Berg und Huettenmännische Monatshefte*, 2009, vol. 154, pp. 346–53.
5. A. Grill and J.K. Briamcombe: *Ironmaking Steelmaking*, 1976, vol. 2, pp. 76–79.
6. Y. Maehara, K. Yasumoto, H. Tomono, T. Nagamichi, and Y. Ohmori: *Mater. Sci. Technol.*, 1990, vol. 6, pp. 793–806.
7. R. Pierer and C. Bernhard: *Materials Science and Technology*, Cincinnati, 2006.
8. G. Xia, C. Bernhard, S. Ilie, and C. Fürst: *6th European Conference on Continuous Casting*, Riccione, Italy, 2008.
9. A. Jablonka, K. Harste, and K. Schwerdtfeger: *Steel Res.*, 1991, vol. 62 (1), pp. 24–33.
10. FactSage: Version 6.2, Database FSstel, Thermfact and GTT-Technologies, 2010.
11. M. Tisza: *Physical Metallurgy for Engineers*, ASM Metals Park Ohio, 2001.
12. ThermoCalc: Version 5, Database TCFE 6, Thermo-Calc Software, 2010.
13. J. Chipman: *Metals Handbook*, ASM Metals Park Ohio, 1973.
14. R. Sriniuasan: *Engineering Materials and Metallurgy*, Tarta Mc Grawhill Education Private Ltd, India, 2010.
15. G. Xia: *Habilitation Treatise*, Chair of Metallurgy, University of Leoben, 2011.
16. T. Emi and H. Fredriksson: *Mater. Sci. Eng.*, 2005, vols. A413–414, pp. 2–9.
17. G. Xia, H.P. Narzt, C. Furst, K. Morwald, J. Moertl, P. Reisinger, and L. Lindenberger: *Ironmak. Steelmak.*, 2004, vol. 31 (5), pp. 364–70.
18. M. Wolf: *Continuous Casting Volume Nine*, Zürich, Switzerland, 1997, pp. 59–68.
19. A.A. Howe: *Appl. Sci. Res.*, 1987, vol. 44, pp. 51–59.
20. A. Kagawa and T. Okamoto: *Mater. Sci. Technol.*, 1986, vol. 2, pp. 998–1008.
21. K. E. Blazek, O. Lanzi Iii, P. L. Gano, and D. L. Kellogg: *AISTech 2007*, Indianapolis, 2007.
22. MTDat: *Phase Diagram Software*, The National Physical Laboratory, Version 5.1, 2012.
23. PANDAT: *PanPhase Diagramm*, CompuTherm LLC, 2012.
24. J. Lacaze and B. Sundman: *Metall. Trans. A*, 1991, vol. 22A, pp. 2211–23.

25. J. Miettinen: *CALPHAD*, 1998, vol. 22 (2), pp. 231–56.
26. D. Connetable, J. Lacaze, P. Maugis, and B. Sundman: *CALPHAD*, 2008, vol. 32 (2), pp. 361–70.
27. G.W. Höhne, H.W. Hemminger, and H.J. Flammersheim: *Differential Scanning Calorimetry: An Introduction for Practitioners*, Springer, Berlin, 1996.
28. W.J. Boettinger, U.R. Kattner, K.-W. Moon, and J.H. Perepezko: *DTA and Heat-flux DSC Measurements of Alloy Melting and Freezing*, NIST Recommended Practice Guide, Special Publication 960-15, 2006.
29. Software: *NETZSCH DSC/DTA Corrections*, Version 2006.01, Netzsch-Gerätebau, 2006.
30. H. Yin, T. Emi, and H. Shibata: *ISIJ Int.*, 1998, vol. 38 (8), pp. 794–801.
31. N.J. McDonald and S. Sridhar: *J. Mater. Sci.*, 2005, vol. 40 (9–10), pp. 2411–16.
32. M. Reid, D. Phelan, and R. Dippenaar: *ISIJ Int.*, 2004, vol. 44 (3), pp. 565–72.
33. D. Phelan, M. Reid, and R. Dippenaar: *Metall. Mater. Trans. A*, 2006, vol. 37A, pp. 985–94.